*Progress In Electromagnetics Research, PIER 97, 291–325, 2009*

# HIGH FREQUENCY SCATTERING BY AN IMPENETRABLE SPHERE

**W. E. I. Sha and W. C. Chew** †

Department of Electrical and Electronic Engineering
The University of Hong Kong
Pokfulam Road, Hong Kong, China

**Abstract**—The high frequency scattering of a scalar plane wave from an impenetrable sphere with a diameter of several thousand wavelengths is treated by the Sommerfeld-Watson transformation, the saddle-point technique (SPT), and the numerical steepest descent method (NSDM). Both the near and far fields for the sphere are computed within the observation angle range of 0 to 180 degree. First, with the aid of the Watson transformation, the fast-convergent residue series replacing the slow-convergent Mie series is derived. Second, a new algorithm for finding the zeros of the Hankel functions is developed. Third, a novel NSDM, which is adaptive to frequency and is hence frequency independent, is proposed to overcome the breakdown of the traditional SPT in the transition region. Numerical results show that when the observation angle is very small, the Mie series solution of the near-field will not be accurate due to error accumulation. Furthermore, using the proposed methods, the CPU times for both the near-field and far-field calculations are frequency independent with controllable error. This work can be used to benchmark future works for high-frequency scattering.

## 1. INTRODUCTION

Mie series solution for scattering from an impenetrable sphere has been known for a long time [1, 2]. Unfortunately, the Mie series will become inefficient at high frequencies due to its slow convergence. Hence, a large number of summation terms must be used to obtain accurate results for both near-field and far-field analyses. The number of terms is proportional to $ka$ (where $k$ is the wavenumber and $a$ is the radius of

Corresponding author: W. E. I. Sha (wsha@eee.hku.hk).
† W. C. Chew is on leave of absence from the University of Illinois, Urbana-Champaign, USA.

sphere) for plane wave incidence and $k^2a^2$ for spherical or cylindrical wave incidence, which leads to expensive computational cost as the frequency increases. An effective method for solving the problem is to make use of Sommerfeld-Watson transformation [3, 4]. It can convert the slow-convergent Mie series to a fast-convergent residue series.

For Watson transformation, many researchers have done good work. Nussenzveig gave a complete discussion about the topic and derived relevant mathematical equations [5]. Rumerman applied the Sommerfeld-Watson transformation to the scattering of acoustic-waves obliquely incident upon cylindrical-shells [6]. Kim [7], and Shim and Kim [8] used the Watson transformation to analyze the scattering of a coated sphere. Paknys [9], and Paknys and Jackson [10] studied a variety of asymptotic expansions of Hankel functions and used the Watson transformation to explain the behaviors of complex waves. Li and Chew [11] gave a new residue series solution of Watson transformation. Valagiannopoulos reviewed the theory and further discussed the initial guess values for the zeros of Hankel functions [12]. Sen and Kuzuoglu used the modified Watson transformation to analyze the high frequency scattering from a double negative cylinder [13].

However, seldom did papers focus on an accurate and efficient zero-finding algorithm. In [7, 8], the authors said the zeros could be found by the Newton-Raphson method but they did not give any numerical implementations. In [12], the authors employed the commercial software Mathematica to solve the problem. Furthermore, the way to efficiently and accurately compute the near-field in the transition region was seldom reported. In addition, the numerical results for the scattering by very large spheres could not be found in the literature.

In this paper, we will address these problems and present the numerical solution of scattering by an impenetrable sphere with a diameter of one thousand wavelength. For the completeness of the paper, mathematical equations and the corresponding physical interpretations will be reviewed. This work can be used to benchmark future works in frequency-independent methods [14–16].

## 2. THEORY

### 2.1. Watson Transformation

The incident plane wave can be expanded as

$$\Psi_i(r,\theta) = \exp(ikr\cos\theta) = \sum_{l=0}^{\infty}(2l+1)i^l j_l(kr)P_l(\cos\theta) \qquad (1)$$

where $j_l$ is the spherical Bessel function of order $l$ and $P_l(\cos\theta)$ is the $l$-th order Legendre polynomial. According to the fact

$$j_l(kr) = \frac{1}{2}\left[h_l^{(2)}(kr) + h_l^{(1)}(kr)\right] \tag{2}$$

the total field in the presence of sphere can be represented as

$$\begin{aligned}\Psi_t(r,\theta) &= \Psi_i(r,\theta) + \Psi_s(r,\theta) \\ &= \frac{1}{2}\sum_{l=0}^{\infty}(2l+1)i^l\left[h_l^{(2)}(\rho) + S_l(B)h_l^{(1)}(\rho)\right]P_l(\cos\theta)\end{aligned} \tag{3}$$

where the $S$-function $S_l(B)$ is determined by the boundary condition $\Psi_t(a,\theta) = 0$

$$S_l(B) = -h_l^{(2)}(B)/h_l^{(1)}(B) \tag{4}$$

and we have introduced the notations

$$\rho = kr, \quad B = ka \tag{5}$$

Equation (3) is the well-known Mie series solution. Unfortunately, the Mie series converges slowly and the computational costs are expensive as the frequency increases.

Using the Watson transformation, a series summation can be converted into an integral form

$$\sum_{l=0}^{\infty} f\left(l+\frac{1}{2}\right) = \frac{1}{2}\int_C f(\lambda)\frac{\exp(-i\pi\lambda)}{\cos\pi\lambda}d\lambda \tag{6}$$

where $C$ is the contour as shown in Fig. 1. Using (6), the total field can be rewritten as

$$\Psi_t(r,\theta) = \int_C g(\lambda,B,\rho)P_{\lambda-1/2}(\cos\theta)e^{-i\lambda\pi/2}\frac{\lambda}{\cos\pi\lambda}d\lambda \tag{7}$$

where

$$g(\lambda,B,\rho) = \frac{1}{2}\left(\frac{\pi}{2\rho}\right)^{1/2}e^{-i\pi/4}\left[H_\lambda^{(2)}(\rho) - \frac{H_\lambda^{(2)}(B)}{H_\lambda^{(1)}(B)}H_\lambda^{(1)}(\rho)\right] \tag{8}$$

For (7) and (8), $P_{\lambda-1/2}$ is the Legendre function of the first kind and we have employed the relation $h_l(x) = (\pi/2x)^{1/2}H_{l+1/2}(x)$ between spherical and cylindrical Hankel functions.

Considering the following properties

$$P_{-\lambda-1/2}(\cos\theta) = P_{\lambda-1/2}(\cos\theta) \tag{9}$$

$$H_{-\lambda}^{(1)}(x) = e^{i\pi\lambda}H_\lambda^{(1)}(x) \tag{10}$$

$$H_{-\lambda}^{(2)}(x) = e^{-i\pi\lambda}H_\lambda^{(2)}(x) \tag{11}$$

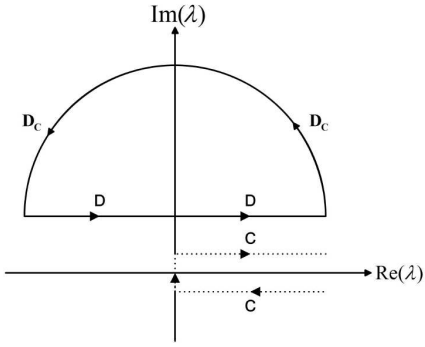


**Figure 1.** The integration paths for Watson transformation.

we find that the integrand of (7) is an odd function of $\lambda$. Hence (7) can be converted to

$$\Psi_t(r,\theta) = \int_{-\infty+i\epsilon}^{\infty+i\epsilon} g(\lambda,B,\rho) P_{\lambda-1/2}(\cos\theta) e^{-i\lambda\pi/2} \frac{\lambda}{\cos\pi\lambda} d\lambda \tag{12}$$

where $\epsilon$ is a small positive number and the contour $C$ is changed to the straight line $D$ above the real axis. Using the identity valid in $D$

$$\frac{e^{-i\lambda\pi/2}}{\cos\pi\lambda} = 2e^{i\lambda\pi/2} \sum_{m=0}^{\infty} (-1)^m e^{2im\pi\lambda} \tag{13}$$

(12) can be rewritten as

$$\begin{aligned} \Psi_t(r,\theta) \;=\; & 2\sum_{m=0}^{\infty} (-1)^m \int_{-\infty+i\epsilon}^{\infty+i\epsilon} g(\lambda,B,\rho) \\ & P_{\lambda-1/2}(\cos\theta) \exp\left[i\pi\lambda(2m+1/2)\right] \lambda d\lambda \end{aligned} \tag{14}$$

The above can be shown to be the same as the result in [11]. To this end, $P_{\lambda-1/2}(\cos\theta)$ can be represented as the summation of the two Legendre functions of the second kind

$$P_{\lambda-1/2}(\cos\theta) = \frac{1}{\pi}\tan\left[\left(\lambda-\frac{1}{2}\right)\pi\right]\left[Q_{\lambda-1/2}(\cos\theta) - Q_{-\lambda-1/2}(\cos\theta)\right] \tag{15}$$

We use the following relations

$$g(-\lambda,B,\rho) = e^{-i\pi\lambda} g(\lambda,B,\rho) \tag{16}$$

and

$$\tan\left[\left(-\lambda-\frac{1}{2}\right)\pi\right] = -\tan\left[\left(\lambda-\frac{1}{2}\right)\pi\right] \tag{17}$$

Equation (14) can be rewritten as

$$\begin{aligned}\Psi_t(r,\theta) &= \frac{2}{\pi}\sum_{m=0}^{\infty}(-1)^m\int_{-\infty+i\epsilon}^{\infty+i\epsilon} g(\lambda,B,\rho)\tan\left[\left(\lambda-\frac{1}{2}\right)\pi\right] \\ &\quad Q_{\lambda-1/2}(\cos\theta)\exp\left[i\pi\lambda(2m+1/2)\right]\lambda d\lambda \\ &\quad +\frac{2}{\pi}\sum_{m=0}^{\infty}(-1)^m\int_{-\infty+i\epsilon}^{\infty+i\epsilon} g(-\lambda,B,\rho)\tan\left[\left(-\lambda-\frac{1}{2}\right)\pi\right] \\ &\quad Q_{\lambda-1/2}(\cos\theta)\exp[-i\pi\lambda(2m+1/2)]\lambda d\lambda \\ &= \frac{2}{\pi}\sum_{m=-\infty}^{\infty}(-1)^m\int_{-\infty+i\epsilon}^{\infty+i\epsilon} g(\lambda,B,\rho)\tan\left[\left(\lambda-\frac{1}{2}\right)\pi\right] \\ &\quad Q_{\lambda-1/2}(\cos\theta)\exp[i\pi\lambda(2m+1/2)]\lambda d\lambda \qquad (18)\end{aligned}$$

We can verify that the Equation (18) has the same form with the equation "(27)" in [11].

If the contribution from the arc of the large semicircle vanishes as its radius approaches infinity, the integration path of (14) can be deformed into the contour $D_c + D$ enclosing the upper half-space with a large semicircle. As a result, we can express (14) as (19)

$$\begin{aligned}\Psi_t(r,\theta) &= 2\sum_{m=0}^{\infty}(-1)^m\oint_{D_c+D} g(\lambda,B,\rho)P_{\lambda-1/2}(\cos\theta) \\ &\quad \exp[i\pi\lambda(2m+1/2)]\lambda d\lambda \qquad (19)\end{aligned}$$

Using Cauchy's residue theorem and considering the first term of (8) is analytic, the contour integral (19) can be deformed as a residue series summation

$$\begin{aligned}\Psi_t(r,\theta) &= 2\pi e^{i\pi/4}\left(\frac{\pi}{2\rho}\right)^{1/2}\sum_{m=0}^{\infty}(-1)^m \\ &\quad \cdot\sum_{n=1}^{\infty} r_n(B)H_{\lambda_n}^{(1)}(\rho)P_{\lambda_n-1/2}(\cos\theta)\exp[i\pi\lambda_n(2m+1/2)]\lambda_n \\ &= \pi e^{i\pi/4}\left(\frac{\pi}{2\rho}\right)^{1/2}\sum_{n=1}^{\infty} r_n(B)H_{\lambda_n}^{(1)}(\rho)P_{\lambda_n-1/2}(\cos\theta) \\ &\quad \frac{\exp(-i\pi\lambda_n/2)}{\cos(\pi\lambda_n)}\lambda_n \qquad (20)\end{aligned}$$

where we have employed (13) again and

$$r_n(B) = \frac{-H_{\lambda_n}^{(2)}(B)}{\frac{\partial H_{\lambda}^{(1)}}{\partial\lambda}(B)\Big|_{\lambda=\lambda_n}} \qquad (21)$$

is the residue terms. Compared with the Mie series solution (3), the residue series solution (20) converges extremely fast at high frequencies. Hence, only the first several terms in (20) are required for numerically accurate solution.

### 2.2. Computing Zeros of Hankel Functions

Computing the zeros of an analytic function in the complex plane is a classical problem in applied mathematics. The pioneering work was done by Delves and Lyness [17]. Kravanja developed the ideas and used the formal orthogonal polynomials to approximate the zeros in the interior of a positively oriented Jordan curve [18–20]. Further, Protopopov proposed a method to locate the zeros of function with large values of derivatives [21]. Based on their work, we propose a novel adaptive scheme to accurately compute the zeros of Hankel functions. Accordingly, the derivative of Hankel functions with respect to the complex order expressed in (21) also can be obtained.

To compute the residue terms (21), one needs: a) find the zeros of Hankel function $H_\lambda^{(1)}(B)$ in the complex $\lambda$-plane. In other words, find $\lambda_n$ subjected to $H_{\lambda_n}^{(1)}(B) = 0$; (b) compute the derivative of the Hankel function with respect to the complex order $\lambda$ at $\lambda = \lambda_n$. Because all the zeros of Hankel functions are simple (first-order zeros), we only consider how to compute these simple zeros in a closed positively oriented Jordan curve.

First, for an analytic function $f(z)$, the number of zeros is determined by the following contour integration

$$N = \oint_C \frac{f'(z)}{f(z)} dz \tag{22}$$

However, in some cases, computing the derivative of the analytic function $f(z)$ is impossible. For example, computing the derivative of Hankel functions with respect to order is difficult. If we write $f(z) = re^{j\theta}$, then $\ln f(z) = \ln r + j\theta$. Using $\frac{d}{dz}[\ln f(z)] = \frac{f'(z)}{f(z)}$ and considering the total change in $\ln r$ is zero, we can express (22) as

$$N = \frac{1}{2\pi} \oint_{C'} d\{\arg[f(z)]\} \tag{23}$$

where $d$ is the variance of argument (phase angle) of $f(z)$. Considering the discontinuities of argument, we use the following analytic form for

computing the variance.

$$d\{\arg[f(z)]\} = d\left\{\arctan\left[\frac{\mathrm{Im}f(z)}{\mathrm{Re}f(z)}\right]\right\} = \frac{1}{|f(z)|^2}\{d[\mathrm{Im}f(z)]\,\mathrm{Re}f(z) - \mathrm{Im}f(z)d[\mathrm{Re}f(z)]\} \quad (24)$$

Using the finite-difference method, we get

$$d\{\arg[f(z_j)]\} = \frac{1}{|f(z_j)|^2}\{[\mathrm{Im}f(z_{j+1}) - \mathrm{Im}f(z_j)]\,\mathrm{Re}f(z_j) - \mathrm{Im}f(z_j)[\mathrm{Re}f(z_{j+1}) - \mathrm{Re}f(z_j)]\} \quad (25)$$

and

$$N = \frac{1}{2\pi}\sum_{j=1}^{p} d\{\arg[f(z_j)]\} \quad (26)$$

where the closed Jordan curve is discretized by the point set $I = \{j|j = 1, 2, \ldots, p\}$ along the anticlockwise orientation.

Next, using the adaptive quadtree decomposition, the closed curve, such as a closed rectangle, can be divided into the smaller closed sub-curves until each sub-curve $c_j$ has a simple pole or no pole. As a result, the analytic function can be expressed as

$$f(z) = P(z)\prod_{j=1}^{s}(z - \zeta_j)^{N_j} \quad (27)$$

where $s$ is the number of sub-curves, $N_j = 0, 1$, and $\sum_{j=1}^{s} N_j = N$. There is no zero in the sub-curve if $N_j = 0$.

Finally, the location of the simple zero can be found by computing the contour integrations

$$\frac{1}{2\pi i}\oint_{c_j}\frac{1}{f(z)} = 1/f'(\zeta_j) \quad (28)$$

$$\frac{1}{2\pi i}\oint_{c_j}\frac{z}{f(z)} = \zeta_j/f'(\zeta_j) \quad (29)$$

where $\zeta_j$ is the simple zero within the closed sub-curve $c_j$. On one hand, according to (28), we can get the derivatives of Hankel functions with respect to the complex order. On the other hand, we also can calculate the locations of zeros $\zeta_j$ by using both (28) and (29). Moreover, Gaussian quadrature or adaptive Simpson quadrature [22] is employed to calculate the contour integration. The Hankel function is evaluated by the uniform asymptotic expansion (A-2).

## 2.3. Near Field

Given the $z$-directed scalar plane wave, the total field of the impenetrable sphere shows different wave behaviors in the shadow, transition, and lit regions as shown in Fig. 2. The mathematical equations and the corresponding physical meanings will be reviewed. In particular, we will discuss the way to compute the total field numerically. The near field condition is $B < \rho \ll B^{4/3}$.

### *2.3.1. Shadow Region*

For the shadow region ($0 \leq \theta < \theta_0, \theta_0 = \arcsin(a/r)$), the total field representation (20) is calculated by using the uniform asymptotic expansion (A-2) and (A-7). The residue term (21) is calculated by (A-2) and the zero-finding algorithm proposed in Section 2.2. The poles $\lambda_n$ in (21) correspond to well known "creeping wave modes" or "Watson modes".

In addition, using (A-4) and (A-8), (20) can be approximated as

$$\Psi_t(r,\theta) \approx (2\pi)^{1/2} \left(\frac{a^2}{r^2-a^2}\right)^{1/4} \frac{\exp\left[ik(r^2-a^2)^{1/2}\right]}{(kr\sin\theta)^{1/2}} \cdot \sum_{m=0}^{\infty}(-1)^m \sum_{n=1}^{\infty} r_n(B)\left[\exp\left(i\lambda_n\gamma_m + i\frac{\pi}{4}\right) + \exp\left(i\lambda_n\delta_m - i\frac{\pi}{4}\right)\right] \quad (30)$$

where

$$\gamma_m = \theta_0 - \theta + 2m\pi \quad (31)$$

$$\delta_m = \theta_0 + \theta + 2m\pi \quad (32)$$

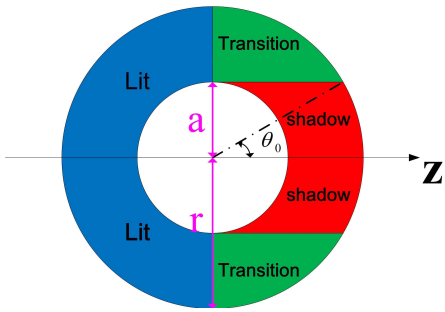


**Figure 2.** The shadow, transition, and lit regions for the $z$-directed incident plane wave. The inner circle and the outer circle denote $R = a$ and $R = r$, respectively.

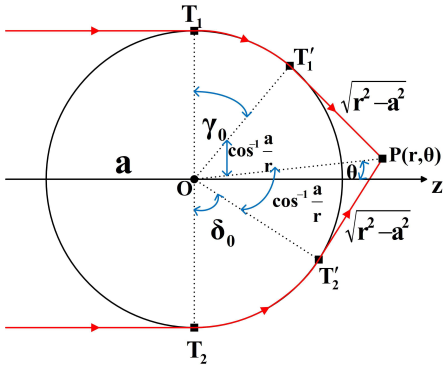


**Figure 3.** Diffraction rays $T_1T_1'P$ and $T_2T_2'P$ reaching a point $P$ in the shadow region.

and $\theta_0 = \arcsin(a/r)$. For (30), it corresponds to the creeping wave traveling along the surface of the sphere and encircling it $m$ times before leaving the surface. The creeping wave travels along the surface with phase velocity slightly smaller than that in free space, due to the delay in overcoming the curvature of the sphere. In particular, the creeping wave experiences a high attenuation rate due to radiation loss. So the leading term ($m = 0$) will make significant contribution. Fig. 3 shows the case. A point $P$ in the shadow region is reached by two rays $T_1T_1'P$ and $T_2T_2'P$. The $T_1'P$ and $T_2'P$ are the tangents to the sphere. In fact, the two rays are also the diffracted rays in geometrical theory of diffraction.

*2.3.2. Lit Region*

For the lit region ($\pi/2 \leq \theta \leq \pi$), the creeping-wave-related terms of $m \geq 1$ in (14) are exponentially small. So we only consider the term of $m = 0$ and the total field can be approximated as

$$\Psi_t(r,\theta) \approx \Psi_t^{(0)}(r,\theta) = 2\int_{-\infty+i\epsilon}^{\infty+i\epsilon} g(\lambda,B,\rho)P_{\lambda-1/2}(\cos\theta)\exp(i\lambda\pi/2)\lambda d\lambda \tag{33}$$

Let us make the splitting

$$P_{\lambda-1/2}(\cos\theta) = Q^{(1)}_{\lambda-1/2}(\cos\theta) + Q^{(2)}_{\lambda-1/2}(\cos\theta) \tag{34}$$

and the terms of $\gamma_0$ and $\delta_0$ in (30) arise from $Q^{(1)}_{\lambda-1/2}$ and $Q^{(2)}_{\lambda-1/2}$, respectively. The term including $Q^{(2)}_{\lambda-1/2}$ remains rapidly convergent

in the lit region. However, the $Q^{(1)}_{\lambda-1/2}$ term increases exponentially and relates to the incident and reflected waves in geometrical optics. As a result, the representation of the total-field (20) by the Watson transformation will break down.

In the lit region, the total field can be represented as the summation of the incident wave and the reflected wave, i.e.,

$$\Psi_t^{(0)}(r,\theta) = \Psi_i + \Psi_r \tag{35}$$

where $\Psi_i$ is the incident wave and $\Psi_r$ is the reflected wave, which can be expressed as

$$\Psi_r = -\left(\frac{\pi}{2\rho}\right)^{1/2} e^{-i\pi/4} \int_\Gamma \frac{H_\lambda^{(2)}(B)}{H_\lambda^{(1)}(B)} H_\lambda^{(1)}(\rho) Q^{(1)}_{\lambda-1/2}(\cos\theta) e^{i\lambda\pi/2} \lambda d\lambda,\ \pi/2 \le \theta \le \pi \tag{36}$$

where the integration path is shown in Fig. 4. Using the asymptotic expansions (A-4) and (A-12) and using the saddle-point technique (SPT), the integral has a single saddle point on the real axis at $\bar{\lambda} = \rho \sin\bar{w} = kp$, where $p = r\sin\bar{w} = a\cos(\frac{\theta-\bar{w}}{2})$. The physical interpretation is shown in Fig. 5. The incident ray that reaches the observation $P$ is reflected at the surface according to the law of geometrical optics. The angle

$$\xi = \frac{1}{2}(\theta - \bar{w}) \tag{37}$$

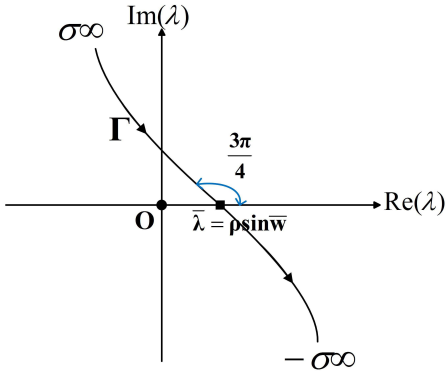


**Figure 4.** The integration path for the reflected wave in the lit region. The $\bar{\lambda} = \rho\sin\bar{w}$ is the saddle point.

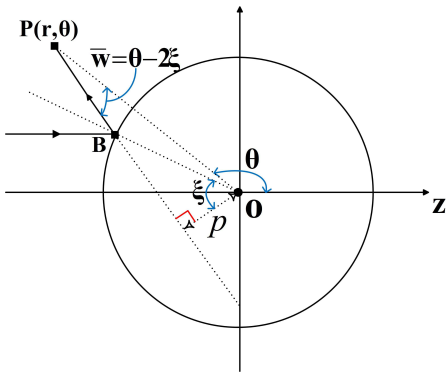


**Figure 5.** The physical interpretation of the saddle point in the lit region: p is the distance from the origin $O$ to the reflected ray $BP$.

is the complement of the incident angle. As a result, it can be found that [5]

$$\Psi_r = -\left[\frac{a^2\sin 2\xi}{4s(s\sin 2\xi + a\cos^3\xi)}\right]^{1/2} \exp\left[ik\left(s - \frac{3}{2}a\sin\xi\right)\right] \cdot \left\{1 + \frac{i}{2B}\left[\frac{1}{\sin^3\xi} + \frac{1}{2^4\sin^2\xi\cos^2\xi}\frac{a}{s} + \frac{3}{2^5}\left(\frac{2}{\sin\xi} - 5\sin\xi\right)\left(\frac{a}{s}\right)^2 - \frac{15}{2^6}\cos^2\xi\left(\frac{a}{s}\right)^3 - \frac{1}{2^3\sin\xi\cos\xi}\cdot\frac{a}{(s\sin 2\xi + a\cos^3\xi)}\right] + O(k^{-2})\right\} \quad (38)$$

where $s = r\cos\bar{w} - \frac{a}{2}\sin\xi$. The first term of (38) represents the reflected wave according to geometrical optics. The second term of (38) represents the correction to geometrical optics corresponding to the second-order WKB approximation.

### *2.3.3. Transition Region*

For the transition region ($\theta_0 \le \theta < \pi/2$), we deform the integral path of the Equation (14) into the path $\Gamma'$ as shown in Fig. 6. The integral containing $H_\lambda^{(2)}(\rho)$ will vanish, since the contour may be closed at infinity and the integrand has no singularity within it [5]. Finally, we get

$$\Psi_t^{(0)} = -\left(\frac{\pi}{2\rho}\right)^{1/2} e^{-i\pi/4}\int_{\Gamma'}\frac{H_\lambda^{(2)}(B)}{H_\lambda^{(1)}(B)}H_\lambda^{(1)}(\rho) Q_{\lambda-1/2}^{(1)}(\cos\theta)e^{i\lambda\pi/2}\lambda d\lambda,\ \theta < \pi/2 \quad (39)$$

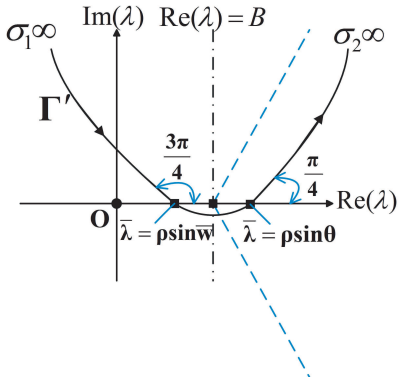


**Figure 6.** The integration path $\Gamma'$ goes through the saddle points $\bar{\lambda} = \rho \sin \bar{w}$ and $\bar{\lambda} = \rho \sin \theta$ (transition region). The dashed lines leaving the real $\lambda$ axis at the angles of $\pm\pi/3$ denote the Stokes lines of the Hankel functions $H_\lambda^{(1,2)}(B)$.

It is noted that the integrand of (39) has the same form with that of (36). However, their integration paths are different. The integration path $\Gamma'$ goes through the two different saddle points. The left one makes a contribution to the reflected wave $\Psi_r$ and is the same as the saddle point in Fig. 4. The right one makes a contribution to the incident wave $\Psi_i$. At the left of the Stokes lines shown in Fig. 6, we have

$$\frac{H_\lambda^{(2)}(B)}{H_\lambda^{(1)}(B)} \sim \exp\left\{-2i\left[(B^2-\lambda^2)^{1/2} - \lambda\cos^{-1}\left(\frac{\lambda}{B}\right) - \frac{\pi}{4}\right]\right\} = \exp(\Phi_1) \tag{40}$$

where

$$\Phi_1 = -2i\left[(B^2-\lambda^2)^{1/2} - \lambda\cos^{-1}\left(\frac{\lambda}{B}\right) - \frac{\pi}{4}\right] \tag{41}$$

The SDP of $\Psi_t^{(0)}$ is the same as that in the lit region (Fig. 4). However, the SDP cannot be extended to infinity at the lower half-plane, because the integral does not converge [5]. At the right of the Stokes lines, we have

$$\frac{H_\lambda^{(2)}(B)}{H_\lambda^{(1)}(B)} \approx -1. \tag{42}$$

The relevant SDP leaves the real $\lambda$ axis at the angle of $\pi/4$. To better understand how the saddle points evolve, the contour plot of the integrand for (36) or (39) is shown in Fig. 7. We find the saddle point

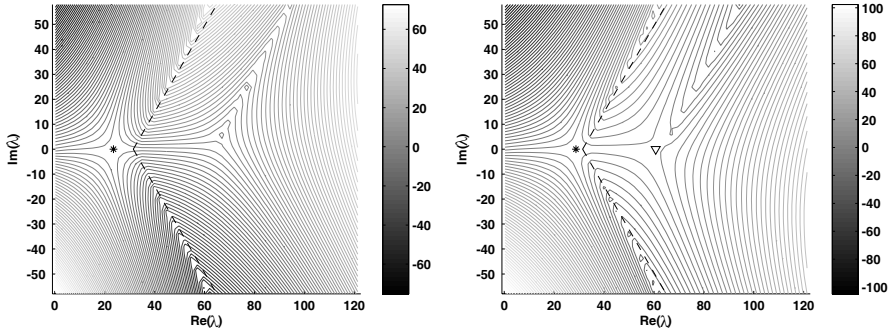


(a) $\theta = 105^{\circ}$ (b) $\theta = 75^{\circ}$

**Figure 7.** The contour of the integrand: $B = 10\pi$. The left stars denote the saddle-points corresponding to the reflected waves, and the right triangle denotes the saddle-point corresponding to the incident wave. The dashed lines denote the Stokes lines of Hankel functions.

corresponding to the incident wave disappears when the observation angle $\theta > \pi/2$. This is the reason why the integration path of the transition region is different from that of the lit region. This is also the reason why (39) represents the total-field; however, (36) represents the reflected field. In addition, the reflected-field solution in the transition region is just the continuation of that in the lit region.

However, as the observation angle $\theta$ approaches $\theta_0$ the shadow boundary, three things will happen: (1) the two saddle points approach each other, moving towards the point $\lambda = B$; (2) the reflected ray and the incident ray meet at the same line called focal line; (3) the Debye asymptotic expansions (A-4) are not available for $H_{\lambda}^{(1)}(B)$ and $H_{\lambda}^{(2)}(B)$. As a result, the expression of reflected wave (38) will diverge, as is the case for geometrical optics approximation.

In the neighborhood of the shadow boundary, the main contribution to the integral arises from the neighborhood of $\lambda = B$.

Thus, we can split the integral into the following form [5]

$$\begin{aligned}\Psi_t^{(0)} &= -\left(\frac{\pi}{2\rho}\right)^{1/2} e^{-i\pi/4}\left[\int_{\sigma_1\infty}^{B} \frac{H_\lambda^{(2)}(B)}{H_\lambda^{(1)}(B)} H_\lambda^{(1)}(\rho) Q_{\lambda-1/2}^{(1)}(\cos\theta) e^{i\lambda\pi/2}\lambda d\lambda\right. \\ &\quad + \int_{B}^{\sigma_2\infty}\left(1+\frac{H_\lambda^{(2)}(B)}{H_\lambda^{(1)}(B)}\right) H_\lambda^{(1)}(\rho) Q_{\lambda-1/2}^{(1)}(\cos\theta) e^{i\lambda\pi/2}\lambda d\lambda \\ &\quad \left. - \int_{B}^{\sigma_2\infty} H_\lambda^{(1)}(\rho) Q_{\lambda-1/2}^{(1)}(\cos\theta) e^{i\lambda\pi/2}\lambda d\lambda\right] \\ &= -\left(\frac{\pi}{2\rho}\right)^{1/2} e^{-i\pi/4}\Big(\Psi_{ta}+\Psi_{tb}+\Psi_{tc}\Big) \end{aligned} \tag{43}$$

where

$$\Psi_{ta} = \int_{\sigma_1\infty}^{B} \frac{H_\lambda^{(2)}(B)}{H_\lambda^{(1)}(B)} H_\lambda^{(1)}(\rho) Q_{\lambda-1/2}^{(1)}(\cos\theta) e^{i\lambda\pi/2}\lambda d\lambda \tag{44}$$

$$\Psi_{tb} = \int_{B}^{\sigma_2\infty}\left(1+\frac{H_\lambda^{(2)}(B)}{H_\lambda^{(1)}(B)}\right) H_\lambda^{(1)}(\rho) Q_{\lambda-1/2}^{(1)}(\cos\theta) e^{i\lambda\pi/2}\lambda d\lambda \tag{45}$$

$$\Psi_{tc} = -\int_{B}^{\sigma_2\infty} H_\lambda^{(1)}(\rho) Q_{\lambda-1/2}^{(1)}(\cos\theta) e^{i\lambda\pi/2}\lambda d\lambda \tag{46}$$

Using the numerical steepest descent method (NSDM), one can treat the above integral term by term. To solve the oscillatory integral, Huybrechs used the NSDM [23, 24] by using the change of variable $t = g(\lambda)$, i.e.,

$$\int f(\lambda) e^{-g(\lambda)} d\lambda = \int f\left(g^{-1}(t)\right) \frac{1}{g'\left(g^{-1}(t)\right)} e^{-t} dt \tag{47}$$

To evaluate the oscillatory integral, one needs: (1) solve $g(\lambda) = t$ for $\lambda = g^{-1}(t)$; (2) treat the singularity of $\frac{1}{g'(g^{-1}(t))}$. For example, if $g(\lambda) = \lambda^2$, the singularity of $\frac{1}{\sqrt{t}}$ will be introduced. So a generalized Gauss-Laguerre integral method must be adopted. For the large sphere problem, $g(\lambda)$ is very complex, and therefore we developed a novel NSDM to evaluate the integral (43).

For $\Psi_{tc}$, we use (A-4) and (A-12) to find its steepest descent path (SDP). Making the change of variable

$$\lambda = \rho \sin w \tag{48}$$

and the phase factor of the integrand of $\Psi_{tc}$ is given by

$$\exp\left[i\rho\alpha(w,\theta)\right] = \exp\left(i\rho\left[\cos w + (w-\theta)\sin w\right]\right) \tag{49}$$

According to (49), the saddle point is located at $\bar{w} = \theta$ and is the same as the right saddle point in Fig. 6. Using the second-order Taylor expansion, we get

$$\alpha(w, \theta) = \cos\theta + \cos\theta \frac{(w-\theta)^2}{2} \tag{50}$$

The corresponding SDP crosses the real $w$ axis at an angle of $\pi/4$, i.e.,

$$w = \theta + \kappa_1 e^{i\pi/4} \tag{51}$$

The upper integration interval for $\kappa_1$ can be set as $\kappa_1 \in \left[0, \sqrt{\frac{C_1}{\rho\cos\theta}}\right]$ and the constant $C_1 \approx 14$ is evaluated by the numerical experiment.

However, the lower integration interval cannot be set as $\kappa_1 \in \left[-\sqrt{\frac{C_1}{\rho\cos\theta}}, 0\right]$ directly. Because the integral contribution from $\lambda = B$ or $w = \theta_0$ cannot be ignored. When $\theta$ approaches $\theta_0$, the contribution is significant. To locally approximate the SDP around $\theta_0$, the first-order Taylor expansion is used as follows

$$\alpha(w, \theta) = \alpha(\theta_0, \theta) - (\theta - \theta_0)\cos\theta_0(w - \theta_0),\ w \approx \theta_0 \tag{52}$$

The "local" SDP in the neighborhood of $w = \theta_0$ can be written as

$$w = \theta_0 + \kappa_2 e^{i3\pi/2} \tag{53}$$

and the integration interval seems to be taken as $\kappa_2 \in \left[0, \frac{C_2}{\rho\cos\theta_0(\theta-\theta_0)}\right]$. Unfortunately, when $\theta \to \theta_0$, the upper limit of the interval will approach infinity. In other words, the integrand cannot be damped to a very small value as we have expected. Fig. 8 gives the complete integration paths for $\Psi_{tc}$. It can be seen clearly the distances $|\theta_0 - \theta_m|$ and $|\theta_m - \theta|$ will become very small when $\theta \approx \theta_0$. So the integration interval of $\kappa_2$ can be revised as

$$\kappa_2 \in [0, \Lambda_2], \Lambda_2 = \min\left\{\frac{C_2}{\rho\cos\theta_0(\theta-\theta_0)}, \theta - \theta_0\right\} \tag{54}$$

where $C_2 \approx 5.5$. Similarly, the integration interval of $\kappa_1$ can be revised as

$$\kappa_1 \in \left[\Lambda_1, \sqrt{\frac{C_1}{\rho\cos\theta}}\right], \Lambda_1 = \max\left\{-\sqrt{\frac{C_1}{\rho\cos\theta}}, -\frac{\theta-\theta_0}{\cos\frac{\pi}{4}}\right\} \tag{55}$$

When $\theta \gg \theta_0$, the integration interval of $\kappa_1$ is $\left[-\sqrt{\frac{C_1}{\rho\cos\theta}}, \sqrt{\frac{C_1}{\rho\cos\theta}}\right]$ and will become very small if the frequency is very high. The frequency-adaptive settings will make it possible that the integration may be evaluated numerically by the Gauss-Legendre method [22] with a

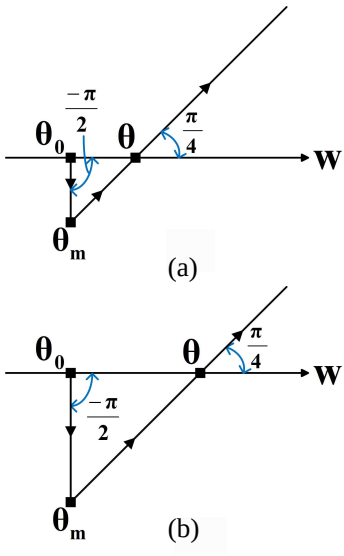


**Figure 8.** The integration paths of $\Psi_{tc}$: (a) $\theta \approx \theta_0$; (b) $\theta \gg \theta_0$.

cost independent of frequency. By (A-4) and (A-12), we find the approximated SDPs and set the integration intervals, but the integrand of $\Psi_{tc}$ should be numerically evaluated by the uniform asymptotic expansions (A-2) and (A-11).

When the observation angle is near to $\theta_0$ ($\theta_0 \leq \theta \leq (\theta_0 + 2A)$), we use the Fock transform [25] to find the SDPs of $\Psi_{ta}$ and $\Psi_{tb}$. According to (A-5), in the neighborhood of $\lambda = B$, we have

$$\frac{H_\lambda^{(2)}(B)}{H_\lambda^{(1)}(B)} \sim \frac{Ai\left(xe^{-2i\pi/3}\right)}{Ai\left(xe^{2i\pi/3}\right)} e^{2i\pi/3} \quad (\lambda < B,\ |\lambda - B| \lesssim B^{1/3}) \tag{56}$$

$$1 + \frac{H_\lambda^{(2)}(B)}{H_\lambda^{(1)}(B)} = \frac{2J_\lambda(B)}{H_\lambda^{(1)}(B)} \sim \frac{Ai\left(x\right)}{Ai\left(xe^{2i\pi/3}\right)} e^{i\pi/3} \quad (\lambda > B,\ |\lambda - B| \lesssim B^{1/3}) \tag{57}$$

where

$$x = A(\lambda - B), \quad A = \left(\frac{2}{B}\right)^{1/3} \tag{58}$$

According to the asymptotic expansion of the Airy function (A-1), we know that the SDPs of $\Psi_{ta}$ and $\Psi_{tb}$ leave the real $x$ axis at the angles

of $2\pi/3$ and 0 respectively.

$$\lambda = B + \frac{\tilde{x}}{A} e^{2i\pi/3}, \quad \tilde{x} = xe^{-2i\pi/3} \tag{59}$$

$$\lambda = B + \frac{\tilde{x}}{A}, \quad \tilde{x} = x \tag{60}$$

Along their SDPs, (56) and (57) are exponentially damped as the form $\exp\left(-\frac{4}{3}\tilde{x}^{3/2}\right)$. Thus we can integrate $\Psi_{ta}$ and $\Psi_{tb}$ along their relevant SDPs with the approximate integration intervals $\tilde{x} \in [0, 8]$ and $\tilde{x} \in [0, 3.5]$, respectively.

When the observation angle moves away from $\theta_0$ ($\theta > (\theta_0 + 2A)$), $\Psi_{tb}$ decreases exponentially but it is not the case for $\Psi_{ta}$. Because $Q^{(1)}_{\lambda-1/2}$ will increase exponentially along the original SDP of $\Psi_{ta}$ leaving the real $x$ axis at the angle of $2\pi/3$. According to (56), (A-1), and (59), the integrand of $\Psi_{ta}$ is dominated by the factor

$$\exp\left(-\frac{4}{3}\tilde{x}^{3/2} + \frac{\sqrt{3}}{2}\frac{\theta}{A}\tilde{x}\right)\exp\left(i\frac{\theta}{2A}\tilde{x}\right) = \exp(\Phi_2)\exp(\Phi_3) \tag{61}$$

where

$$\Phi_2 = -\frac{4}{3}\tilde{x}^{3/2} + \frac{\sqrt{3}}{2}\frac{\theta}{A}\tilde{x} \tag{62}$$

$$\Phi_3 = i\frac{\theta}{2A}\tilde{x} \tag{63}$$

Considering $\tilde{x}$ is real, the integrand oscillates as $\sim \exp\left(i\frac{\theta}{A}\tilde{x}\right)$. Letting $\partial\Phi_2/\partial\tilde{x} = 0$, we know that the integrand has the peak $\tilde{x} \approx (\theta/A)^2$. The similar phenomenon was also found for far-field computation [26]. According to our numerical experiment, we need to change the SDP when $\theta > (\theta_0 + 2A)$.

To find the revised SDP of $\Psi_{ta}$, we use the Debye expansion (A-4) to approximate $H^{(1)}_{\lambda}(\rho)$ and use (A-12) to approximate $Q^{(1)}_{\lambda-1/2}(\cos\theta)$, which are the same as those for the lit region. However, the two saddle points are still close to the point $(B, 0)$, the Fock transform approximations must be used for $H^{(2)}_{\lambda}(B)$ and $H^{(1)}_{\lambda}(B)$, i.e.,

$$\frac{H^{(2)}_{\lambda}(B)}{H^{(1)}_{\lambda}(B)} \sim \exp\left(\frac{\pi}{2}i - \frac{4}{3}\tilde{x}^{3/2}\right) = \exp(\Phi_4) \tag{64}$$

where

$$\Phi_4 = \frac{\pi}{2}i - \frac{4}{3}\tilde{x}^{3/2} \tag{65}$$

From the above analysis, we need only to compare the phase $\Phi_4$ with the phase $\Phi_1$ in (41) to observe the differences in the transition region and the lit region. For the lit region, according to (40), we get

$$\frac{\partial \Phi_1}{\partial \lambda} = 2i \arccos\left(\frac{\lambda}{B}\right) \approx i\pi \left(1 - \frac{\lambda}{B}\right)^{1/2} \tag{66}$$

For the transition region and when $\theta > (\theta_0 + 2A)$, we get

$$\frac{\partial \Phi_4}{\partial \lambda} = i2^{3/2} \left(1 - \frac{\lambda}{B}\right)^{1/2} \tag{67}$$

The above, together with the derivation of the remaining phases in the integrand, determines the location of the saddle point. In view of the fact that $2^{3/2} \approx \pi$, hence the location of the saddle point for $\Psi_{ta}$ is almost same as shown in Fig. 4 or shown in Fig. 6 (left one). We also have

$$\frac{\partial^2 \Phi_1}{\partial \lambda^2} = \frac{-2i}{(B+\lambda)^{1/2}(B-\lambda)^{1/2}} \tag{68}$$

and

$$\frac{\partial^2 \Phi_4}{\partial \lambda^2} = \frac{-\sqrt{2}i}{B^{1/2}(B-\lambda)^{1/2}} \tag{69}$$

The above, together with the derivation of the remaining phases, when evaluated at $\lambda = \bar{\lambda}$, determines the direction of the SDP. If $\bar{\lambda} \approx B$, (68) and (69) are still comparable.

According to the above analysis, we can deform the integration path as shown in Fig. 9. Obviously, the integration path will pass through the end point $x = 0$ and the saddle point $\bar{x} = A(\bar{\lambda} - B)$, where $\bar{\lambda}$ is the left saddle point in Fig. 6 or the saddle point in Fig. 4. Using the tricks similar to (54) and (55), the integration intervals for the saddle point and the end point are, respectively,

$$x \in \left[\max\left\{-C_3, -\frac{C_4}{\cos(\pi/4)}\right\}, C_3\right] e^{3i\pi/4} \tag{70}$$

and

$$x \in [0, \min\{C_4, C_5\}]\, e^{3i\pi/2} \tag{71}$$

where $C_3 \approx 3.8(\theta/A)^{1/2}$, $C_4 = |\bar{x}|$, and $C_5 \approx 1.9(\theta/A)^{1/2}$. As the frequency increases, the integration intervals will be slightly extended for a fixed observation angle. Fortunately, the available range of the lit region solution (38) will be extended to the smaller angles also. So, we need not increase the number of integration nodes as the frequency increases.

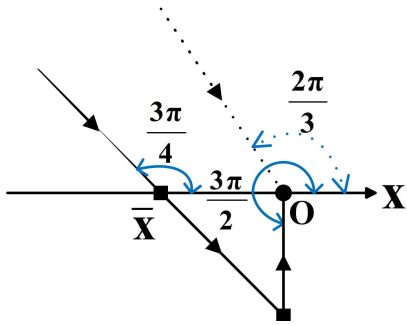


**Figure 9.** The integration paths of $\Psi_{ta}$. When the observation angle $\theta_0 \leq \theta \leq (\theta_0 + 2A)$, the path (dotted) leaves the real axis at the angle of $2\pi/3$ and goes to the end point $x = 0$. When the observation angle $\theta > (\theta_0 + 2A)$, the revised path path (solid) goes through the left saddle point related to the reflected wave and the end point $x = 0$. For the numerical implementation, we integrate $\Psi_{ta}$ along the opposite direction and reverse the sign of the summation.

### 2.4. Far Field

For $r \to \infty$, we have

$$\Psi_t(r,\theta) = e^{ikz} + f_s(k,\theta)\frac{e^{ikr}}{r} \tag{72}$$

where $f_s(k,\theta)$ is the scattering amplitude.

From Fig. 5, the angle $\bar{w}$ will approach zero as $r \to \infty$, so that $\xi \to \theta/2$ in (37) and the saddle point approaches $\bar{\lambda} = kp = B\cos(\theta/2)$. As a result, the reflected ray travels along $\theta$ direction. Using the large argument expansion of the Hankel function (A-6) and (36), the scattering amplitude can be approximated as

$$f_s(k,\theta) \approx f_r(k,\theta) = \frac{i}{k}\int_\Gamma \frac{H_\lambda^{(2)}(B)}{H_\lambda^{(1)}(B)} Q_{\lambda-1/2}^{(1)}(\cos\theta)\lambda d\lambda,\ \theta \gg 0 \tag{73}$$

where $f_r$ is the reflection amplitude. The integration path $\Gamma$, which is parallel to the integration path in Fig. 4, crosses the real axis at the saddle point $\bar{\lambda} = B\cos(\theta/2)$ with an angle of $-\pi/4$. Using the asymptotic expansions (A-4) and (A-12) and using the SPT, we can

get [26]

$$f_r(k,\theta) = -\frac{a}{2}\exp\left(-2iB\sin\frac{\theta}{2}\right)\left(1+\frac{i}{2B\sin^3\frac{\theta}{2}} + \frac{2+3\cos^2\frac{\theta}{2}}{\left(2B\sin^3\frac{\theta}{2}\right)^2} + O\left[\left(2B\sin^3\frac{\theta}{2}\right)^{-3}\right]\right) \tag{74}$$

The expression agrees with the well-known conclusion in electromagnetics and optics that the backward radar cross section (RCS) of the large sphere is about $\pi a^2$. Recall that the solution (38) will diverge when the observation angle $\theta \to \theta_0$ the shadow boundary. Likewise, (74) will break down when $\theta \to \theta_0 = 0$. Additionally, the contribution from creeping wave cannot be ignored when $\theta$ approaches 0.

Hence, an alternative integral representation should be used. Let us start by the partial-wave expansion of $f_s(k,\theta)$ obtainable from (3), the Mie series solution by letting $\rho \to \infty$

$$f_s(k,\theta) = \sum_{l=0}^{\infty} \frac{2l+1}{2ik}\left[S_l(k)-1\right]P_l(\cos\theta) \tag{75}$$

where $S_l$ is given by (4). According to the Poisson's summation formula

$$\sum_{l=0}^{\infty} f\left(l+\frac{1}{2}\right) = \sum_{m=-\infty}^{\infty}(-1)^m \int_0^{\infty} f(\lambda)e^{2im\pi\lambda}d\lambda \tag{76}$$

(75) can be represented as

$$f_s(k,\theta) = \frac{i}{k}\sum_{m=-\infty}^{\infty}(-1)^m \int_0^{\infty}[1-S(\lambda,k)]P_{\lambda-1/2}(\cos\theta)e^{2im\pi\lambda}\lambda d\lambda \tag{77}$$

where $S(\lambda,k) = -H_\lambda^{(2)}(B)/H_\lambda^{(1)}(B)$. In view of the fact

$$S(-\lambda,k) = e^{2i\pi\lambda}S(\lambda,k) \tag{78}$$

we make $\lambda \to -\lambda$ in the sum from $m=-1$ to $-\infty$ and get

$$f_s(k,\theta) = \frac{i}{k}\sum_{m=0}^{\infty}(-1)^m\left\{\int_{-\infty}^{0}\left[e^{2i\pi\lambda}-S(\lambda,k)\right]P_{\lambda-1/2}(\cos\theta)e^{2im\pi\lambda}\lambda d\lambda + \int_0^{\infty}\left[1-S(\lambda,k)\right]P_{\lambda-1/2}(\cos\theta)e^{2im\pi\lambda}\lambda d\lambda\right\} \tag{79}$$

Because the integrand of the first integral in (79) goes to zero exponentially for $|\lambda| \to \infty$ in the second quadrant, we may shift

the path of integration to the positive imaginary axis, from $i\infty$ to 0. Writing

$$e^{2i\pi\lambda} - S(\lambda,k) = e^{2i\pi\lambda} - 1 + 1 - S(\lambda,k) \tag{80}$$

(79) can be simplified as

$$\begin{aligned} f_s(k,\theta) = & \frac{i}{k}\sum_{m=0}^{\infty}(-1)^m \int_{i\infty}^{0} \left[e^{2i\pi\lambda}-1\right] P_{\lambda-1/2}(\cos\theta) e^{2im\pi\lambda}\lambda d\lambda \\ & + \frac{i}{k}\int_0^{\infty} [1-S(\lambda,k)]\, P_{\lambda-1/2}(\cos\theta)\lambda d\lambda \\ & + \frac{i}{k}\int_{i\infty}^{0} [1-S(\lambda,k)]\, P_{\lambda-1/2}(\cos\theta)\lambda d\lambda \\ & + \frac{i}{k}\sum_{m=1}^{\infty}(-1)^m \int_C [1-S(\lambda,k)]\, P_{\lambda-1/2}(\cos\theta) e^{2im\pi\lambda}\lambda d\lambda \end{aligned} \tag{81}$$

where $C$ is the path going from $i\infty$ to 0 and from 0 to $\infty$. The last term of (81) corresponds to the high-order Watson modes ($m \geq 1$) which are exponentially small in the high frequency limit. The creeping waves corresponding to $m = 0$ have been considered in the first three terms.

Next, we ignore the last term in (81) and employ the identity

$$\sum_{m=1}^{\infty}(-1)^m \left(e^{2i\pi\lambda}-1\right) e^{2im\lambda\pi} = e^{2i\pi\lambda}\left(\frac{2}{1+e^{2i\pi\lambda}}-1\right) \tag{82}$$

Then we get

$$\begin{aligned} f_s(k,\theta) \approx & \frac{i}{k}\int_0^{\infty}[1-S(\lambda,k)]P_{\lambda-1/2}(\cos\theta)\lambda d\lambda \\ & - \frac{i}{k}\int_{i\infty}^{0} S(\lambda,k) P_{\lambda-1/2}(\cos\theta)\lambda d\lambda \\ & + \frac{2i}{k}\int_{i\infty}^{0} \frac{e^{2i\pi\lambda}}{1+e^{2i\pi\lambda}} P_{\lambda-1/2}(\cos\theta)\lambda d\lambda \end{aligned} \tag{83}$$

Using the similar split method in (43), the scattering amplitude $f_s$ can be represented as [26]

$$f_s(k,\theta) \approx f_{sa} + f_{sb} + f_{sc} \tag{84}$$

where

$$\begin{aligned} f_{sa} + f_{sb} = & \frac{i}{k}\left(\int_{i\infty}^{0} + \int_0^B\right) \frac{H_\lambda^{(2)}(B)}{H_\lambda^{(1)}(B)} P_{\lambda-1/2}(\cos\theta)\lambda d\lambda \\ & + \frac{i}{k}\int_B^{\infty}\left(1+\frac{H_\lambda^{(2)}(B)}{H_\lambda^{(1)}(B)}\right) P_{\lambda-1/2}(\cos\theta)\lambda d\lambda \end{aligned} \tag{85}$$

and

$$f_{sc}=\frac{i}{k}\int_0^B P_{\lambda-1/2}(\cos\theta)\lambda d\lambda+\frac{2i}{k}\int_{i\infty}^0 \frac{e^{2i\pi\lambda}}{1+e^{2i\pi\lambda}}P_{\lambda-1/2}(\cos\theta)\lambda d\lambda \quad (86)$$

For $f_{sc}$, we can use the analytical method to evaluate its value [26]. When the observation angle $0 \leq \theta \leq 2A$, we use the same Fock transforms (56) and (57) as those for the near-field calculations. Hence the SDPs of $f_{sa}$ and $f_{sb}$, which are the same as those of $\Psi_{ta}$ and $\Psi_{tb}$, leave the real $x$ axis at the angles of $2\pi/3$ and 0, respectively. Notice from (58) that $A$ becomes increasingly small at higher frequencies.

However, when the observation angle $\theta > 2A$, the SDP of $f_{sa}$ should be changed. The integral $f_{sa}$ can be split as

$$\begin{aligned} f_{sa} \;=\; f_{sa}^{(1)}+f_{sa}^{(2)} &= \frac{i}{k}\int_{i\infty}^B \frac{H_\lambda^{(2)}(B)}{H_\lambda^{(1)}(B)}Q_{\lambda-1/2}^{(1)}(\cos\theta)\lambda d\lambda \\ &+\frac{i}{k}\int_{i\infty}^B \frac{H_\lambda^{(2)}(B)}{H_\lambda^{(1)}(B)}Q_{\lambda-1/2}^{(2)}(\cos\theta)\lambda d\lambda \end{aligned} \quad (87)$$

For $f_{sa}^{(2)}$, the term $Q_{\lambda-1/2}^{(2)}$ will decrease exponentially along the original SDP leaving the real $x$ axis at the angle of $2\pi/3$. For $f_{sa}^{(1)}$, the term $Q_{\lambda-1/2}^{(1)}$ will increase exponentially. According to (66), (67), (68), and (69), we have verified that the Fock transform and the Debye expansion for $H_\lambda^{(2)}(B)/H_\lambda^{(1)}(B)$ are comparable. In addition, the integrand of $f_{sa}^{(1)}$ is the same as that of $f_r(k,\theta)$ in (73), whose SDP crosses the real axis at the saddle point $\bar{\lambda}=B\cos(\theta/2)$ with an angle of $-\pi/4$. Hence, the integration path of $f_{sa}^{(1)}$ is changed as shown in Fig. 9 when $\theta > 2A$. The mathematical models and the numerical methods for $f_{sa}$ and $f_{sb}$ are almost same as those for $\Psi_{ta}$ and $\Psi_{tb}$.

### 2.5. Mie Series

For the Mie series solutions, we can use the recurrence equations [27] to accelerate the calculations of Hankel functions and Legendre functions.

$$H_{l+1}^{(1,2)}(z) \;=\; -H_{l-1}^{(1,2)}(z)+\frac{2l}{z}H_l^{(1,2)}(z) \quad (88)$$

$$P_{l+1}(z) \;=\; \frac{1}{l+1}\Big[(2l+1)zP_l(z)-lP_{l-1}(z)\Big] \quad (89)$$

The number of the summation terms for the near-field and the far-field computations are, respectively, $l_n = \rho + C_6\rho^{1/3} + C_7$ and $l_f = B + C_6B^{1/3} + C_7$. According to [28], $C_6 \approx 4$ and $C_7 \approx 2$. Considering

the Hankel functions $H_l^{(1,2)}(B)$ will diverge when $l > l_f$, we use the following approximation for the near-field computation

$$\frac{H_l^{(2)}(B)}{H_l^{(1)}(B)} \approx -1, \quad l > B + C_6 B^{1/3} + C_7 \tag{90}$$

## 3. NUMERICAL RESULTS

### 3.1. Near Field

We assume that $k = 2\pi$, $a = 500$, and $r = 2a$. As a result, $\theta_0 = 30°$. The searching domain for locating the zeros of Hankel function is taken as $\mathrm{Re}\lambda \in [\mathrm{B}, \mathrm{B} + \mathrm{C_n B}^{1/3}]$ and $\mathrm{Im}\lambda \in [1, \mathrm{C_n B}^{1/3}]$, where the constant $C_n$ is almost equal to the number of zeros. Here, $C_n$ is taken as 8. If $C_n$ is not too large, within the searching domain, the Hankel function can be approximated by the Airy function through the Fock transform (56)–(58). Although the searching domain will be extended as the frequency increases, the oscillations of the Hankel function are unchanged. Hence, the discretization points need not be increased for the difference implementation (25) and the integration implementations (28)–(29). Fig. 10 shows the locations of the first eight zeros of $H_\lambda^{(1)}(B)$, where the zeros $\lambda_n$ are located at the Stokes line of $H_\lambda^{(1)}(B)$ with the approximated slope angle $\pi/3$. According to (30), the wavenumber of the creeping wave modes is $k_c = \lambda_n/a$. From Fig. 10, we can see $\mathrm{Re}(\lambda_n/a) = k_c' > k = B/a$ and therefore the

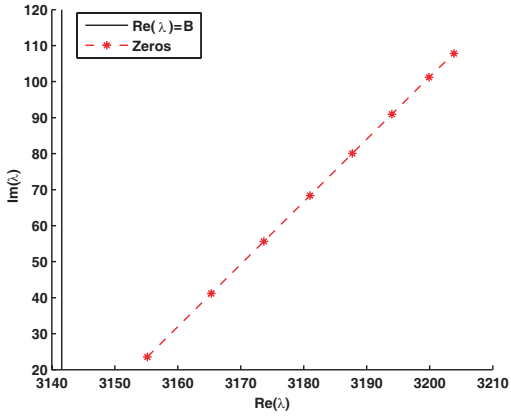


**Figure 10.** The locations of the first eight zeros of $H_\lambda^{(1)}(B)$: $a = 500$ and $k = 2\pi$.

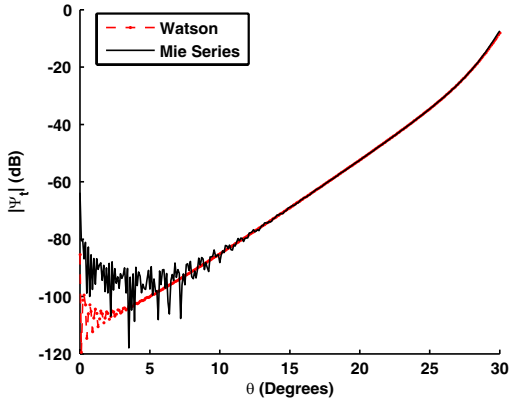


**Figure 11.** The total field in the shadow region: $a = 500$ and $r = 2a$.

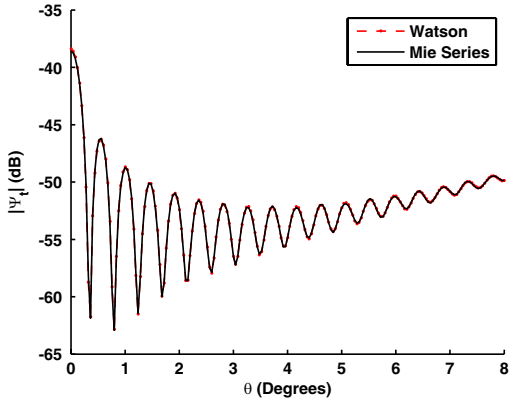


**Figure 12.** The total field in the shadow region: $a = 62.5$ and $r = 2a$.

phase velocity of the creeping waves is smaller than that in free space. The attenuation rate of the creeping waves depends on $k_c'' = \mathrm{Im}(\lambda_n/a)$ and will increase for the high-order creeping wave modes. Fig. 11 shows the solution by the Watson transform. It is noted that when the observation angle approaches 0, the amplitude of the total field is very small due to the fact the scattered field and the incident field have comparable amplitudes but with opposite signs. Because the number of the summation terms for the Mie series is large and the recurrence equations (88)–(89) are used, the error may be accumulated. We change the radius of the sphere as $a = 250/n, n = 1, 2, 4$, and keep $r = 2a$. The near field results by the Watson transform and the Mie series are given in Fig. 12, Fig. 13, and Fig. 14. As the radius increases,

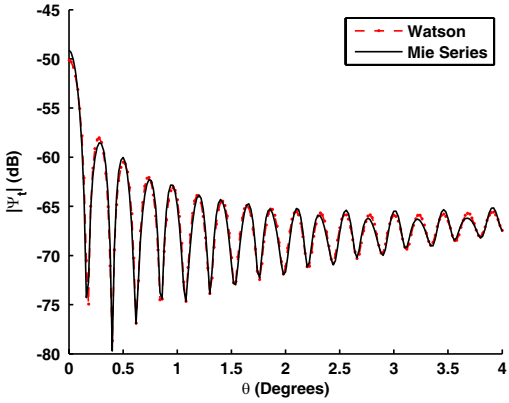


**Figure 13.** The total field in the shadow region: $a = 125$ and $r = 2a$.

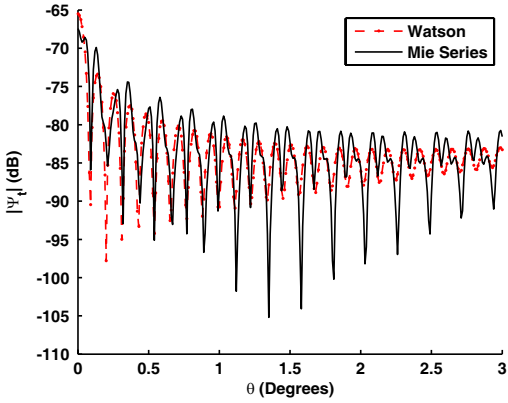


**Figure 14.** The total field in the shadow region: $a = 250$ and $r = 2a$.

the solutions by the Mie series introduce the random noises for the small observation angles.

Figure 15 shows the transition region solution by the NSDM. The solution is accurate between 20° to 65°. Compared with the analytical solution by the Fock transform [5], the accuracy of NSDM is better. Fig. 16 shows the lit region solution by the analytical SPT. The solution is accurate between 55° to 180°. From the figures, it can be seen the NSDM solution by the uniform asymptotic expansion successfully bridges the gap between the lit region solution and the shadow region solution.

The total CPU time by the sum of Watson transform, the NSDM, and the SPT for the near field calculation is given in Fig. 17. The error

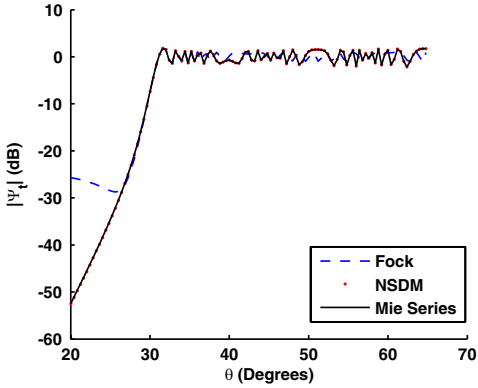


**Figure 15.** The total field in the transition region: $a = 500$ and $r = 2a$. NSDM denotes the numerical steepest descent method, and Fock denotes the analytical Fock transform method [5].

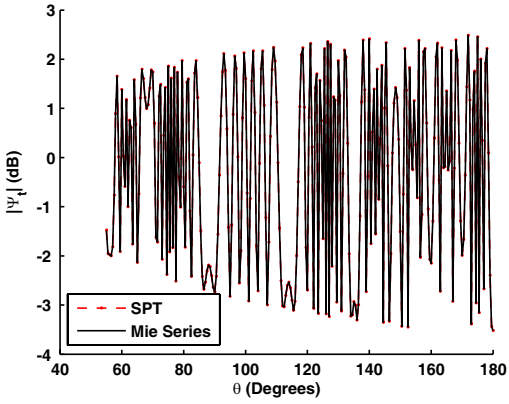


**Figure 16.** The total field in the lit region: $a = 500$ and $r = 2a$. SPT denotes the saddle-point technique.

of the Mie series solution for near-field hardly can be controlled, hence the error comparison is meaningless.

### 3.2. Far Field

We assume that $a = 500$ and $k = 2\pi$. Fig. 18 shows the forward region solution by the NSDM. The solution is accurate between 0° to 50°. Fig. 19 compares our solution with the original solution proposed in [26]. The number of the integration nodes is uniform for the two

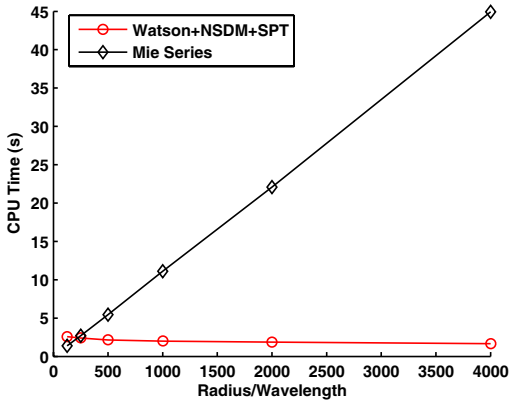


**Figure 17.** The total CPU time for the near field calculation: $a = 500$ and $r = 2a$. The shadow, transition, and lit regions use respectively the Watson transform, the numerical steepest descent method, and the saddle-point technique.

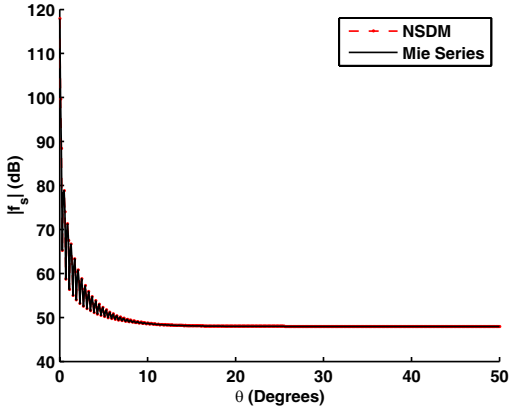


**Figure 18.** The forward region solution of the scattering amplitude for far-field: $a = 500$. The numerical steepest descent method (NSDM) is adopted.

solutions. The original integration path proposed in [26] goes along the real $x$ axis from $x = 0$ to $x = \bar{x}$ and the integrand will become very oscillatory as the observation angle increases. Fig. 20 shows the backward region solution by the SPT. The solution is accurate between 40° to 180°. Hence, the NSDM solution and the SPT solution can overlap with each other. Fig. 21 shows the total CPU time for the far-

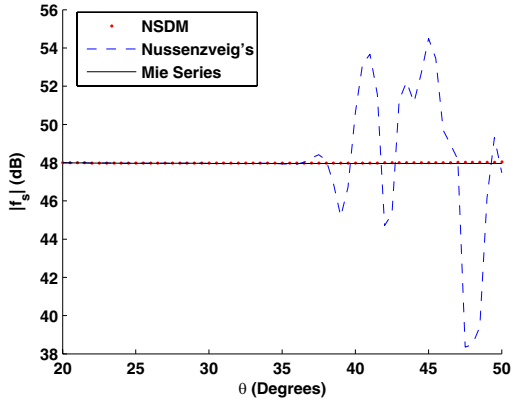


**Figure 19.** The forward region solution of the scattering amplitude for far-field: $a = 500$. The numerical steepest descent method (NSDM) is proposed in this paper, and the original solution by Nussenzveig was proposed in [26].

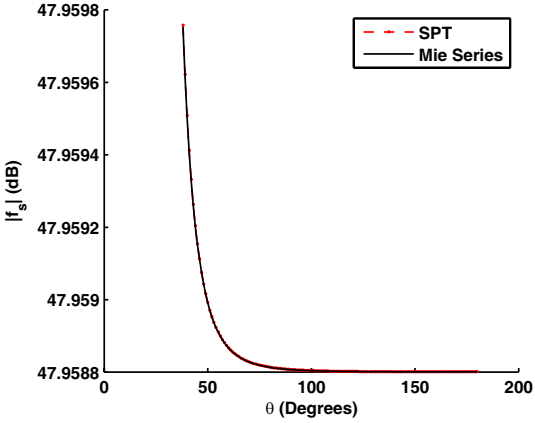


**Figure 20.** The backward region solution of the scattering amplitude for far-field: $a = 500$. The saddle-point technique (SPT) is adopted.

field calculation as a function of the electrical size of the radius. Here, we did not add any integration nodes. Fig. 22 shows the polar plot of the bistatic RCS for the impenetrable sphere. From the figure, as the electrical size of the sphere increases, the forward region becomes very smaller and the RCS result gets more oscillatory. Because the analytical SPT for the backward region is faster than the NSDM for the forward region, the total CPU time slightly decreases. Fig. 23 shows

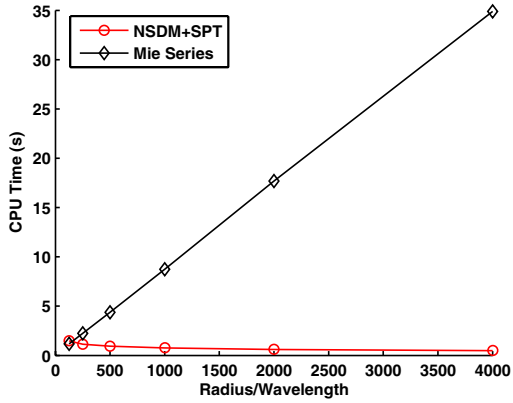


**Figure 21.** The total CPU time for the far-field calculation. The numerical steepest descent method (NSDM) and the saddle-point technique (SPT) are used respectively for the forward region and the backward region.

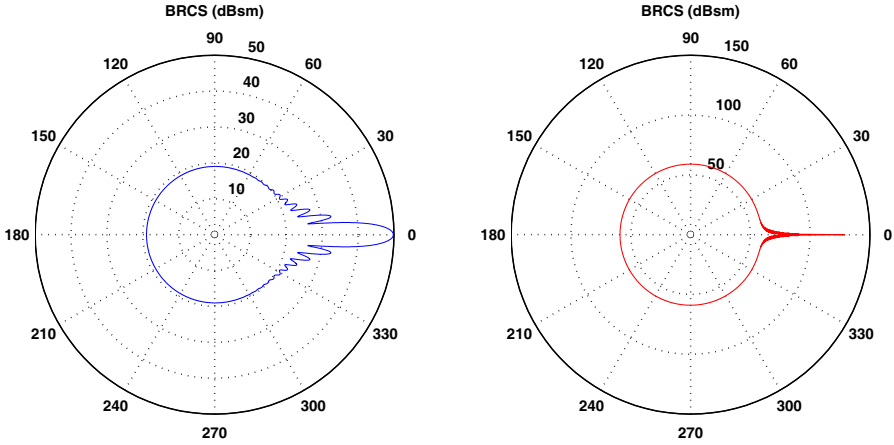


(a) $a = 5$ (b) $a = 500$

**Figure 22.** The bistatic RCS of the impenetrable sphere.

the relative two-norm error. The scattering amplitude is large, hence the accuracy of the Mie series solution can be controlled. We compare our solution with the Mie series solution, and the error decreases as the frequency increases.

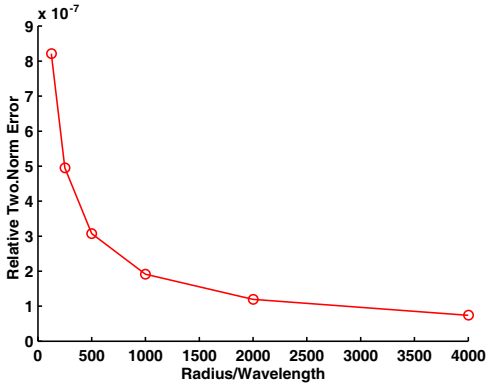


**Figure 23.** The relative two-norm error for the far-field calculation. The Mie series solution is used as reference solution. The numerical steepest descent method (NSDM) and the saddle-point technique (SPT) are used respectively for the forward region and the backward region.

## 4. CONCLUSION

The high frequency scattering of a scalar plane wave from a very large impenetrable sphere is computed.

For the near-field calculation, the Watson transformation, the numerical steepest descent method, and the saddle-point technique are adopted for the shadow, transition, and lit regions. The numerical steepest descent method solution bridges the gap between the Watson transformation solution and the saddle-point technique solution. The zeros of Hankel functions can be effectively and accurately found by the numerical difference and integration methods. The total CPU time is frequency independent. In particular, the Mie series solution is not accurate for the near-field calculation due to the error accumulation.

For the far field calculation, the numerical steepest descent method and the saddle-point technique are adopted for the forward and backward regions. The two solution can overlap with each other. The total CPU time is frequency independent and the numerical error can be controlled compared with the Mie series solution.

## APPENDIX A. THE ASYMPTOTIC EXPANSIONS FOR SPECIAL FUNCTIONS

In this appendix, we will review the asymptotic expansions for special functions [5, 9, 26, 27, 29].

The asymptotic expansion of the Airy function is

$$Ai(z) \sim \frac{\exp\left(-\frac{2}{3}z^{3/2}\right)}{2\sqrt{\pi}z^{1/4}},\ |z| \gg 1\ \ |\arg(z)| < \pi \tag{A-1}$$

The uniform asymptotic expansion of the Hankel function is given by

$$H_\lambda^{(1)}(\lambda z) \sim 2e^{-\pi i/3}\left(\frac{4\xi}{1-z^2}\right)^{1/4}\left\{\frac{Ai\left(e^{2\pi i/3}\lambda^{2/3}\xi\right)}{\lambda^{1/3}}+\right.$$
$$\left.\frac{e^{2\pi i/3}Ai'\left(e^{2\pi i/3}\lambda^{2/3}\xi\right)}{\lambda^{5/3}}\left[-\xi^{-1/2}\sum_{s=0}^{1}V_s\xi^{-3s/2}U_{1-s}\left(\left(1-z^2\right)^{-1/2}\right)\right]\right\} \tag{A-2}$$

where $V_0 = 1$, $V_1 = 5/48$, $U_0(t) = 1$, $U_1(t) = (3t - 5t^3)/24$, and $Ai$ and $Ai'$ are the Airy function and its derivative, which can be numerically evaluated well. The expansion for $H_\lambda^{(2)}(\lambda z)$ can be obtained by changing the sign of $i$ in (A-2). Here, we use the first two terms to obtain more accurate numerical results, which is different from [9] employing only the leading term. In (A-2), the important parameter $\xi$ should be treated carefully and the branch is chosen so that $\xi$ is real when $z$ is positive, i.e.,

$$\begin{aligned}\frac{2}{3}\xi^{3/2} &= \ln\left(\frac{1+\sqrt{1-z^2}}{z}\right) - \sqrt{1-z^2}, \quad |z| \le 1\\ \frac{2}{3}(-\xi)^{3/2} &= \sqrt{z^2-1} - \arccos\left(\frac{1}{z}\right), \quad |z| > 1\end{aligned} \tag{A-3}$$

In addition, all the complex multiple-valued functions in (A-2) and (A-3) are uniquely determined by their principal values. The Debye expansions for the Hankel functions are given by

$$H_\lambda^{(1,2)}(\rho) \sim (2/\pi)^{1/2}\left(\rho^2-\lambda^2\right)^{-1/4}\cdot\left[1 \mp \frac{i}{8\left(\rho^2-\lambda^2\right)^{1/2}}\left(1+\frac{5}{3}\frac{\lambda^2}{\rho^2-\lambda^2}\right)\right]$$
$$\times \exp\left\{\pm i\left[\left(\rho^2-\lambda^2\right)^{1/2} - \lambda\cos^{-1}\frac{\lambda}{\rho} - \frac{\pi}{4}\right]\right\},$$
$$-\rho < \lambda < \rho,\ |\lambda-\rho| > |\lambda|^{1/3} \tag{A-4}$$

The Debye expansions are not available when $|\lambda - \rho|$ becomes comparable with $|\lambda|^{1/3}$. Hence we must employ the following expansions

$$H_\lambda^{(1,2)}(\rho) \sim 2\exp(\mp i\pi/3)\,(2/\lambda)^{1/3}Ai\left[\exp(\pm 2i\pi/3)\,(2/\lambda)^{1/3}(\lambda-\rho)\right] \tag{A-5}$$

Moreover, when $\rho \to \infty$, (A-4) reduces to the large augment expansion of the Hankel functions

$$H_\lambda^{(1,2)}(\rho) \sim \left(\frac{2}{\pi\rho}\right)^{1/2} \exp\left[\pm i\left(\rho - \lambda\frac{\pi}{2} - \frac{\pi}{4}\right)\right],\ \rho \to \infty \tag{A-6}$$

The Szegö-Olver uniform asymptotic expansion for the Legendre function of the first kind is given by

$$P_{\lambda-1/2}(\cos\theta) \sim \left(\frac{\theta}{\sin\theta}\right)^{1/2} \left\{\left[1 + \frac{1}{128\lambda^2}\left(1 - \frac{9}{\sin^2\theta} - 6\frac{\cot\theta}{\theta} + \frac{15}{\theta^2}\right)\right] J_0(\lambda\theta) - \frac{1}{8\lambda}\left(\frac{1}{\theta} - \cot\theta\right) J_1(\lambda\theta)\right\} \tag{A-7}$$

For $|\lambda|\theta \gg 1$, (A-7) becomes

$$P_{\lambda-1/2}(\cos\theta) \sim \left(\frac{2}{\pi\lambda\sin\theta}\right)^{1/2} \cdot \left[\cos\left(\lambda\theta - \frac{\pi}{4}\right)\right],\ |\lambda|\theta \gg 1 \tag{A-8}$$

Similar to the relation $J_\lambda(\rho) = \frac{1}{2}\left[H_\lambda^{(1)}(\rho) + H_\lambda^{(2)}(\rho)\right]$, the Legendre function of the first kind can be represented as

$$P_{\lambda-1/2}(\cos\theta) = Q_{\lambda-1/2}^{(1)}(\cos\theta) + Q_{\lambda-1/2}^{(2)}(\cos\theta) \tag{A-9}$$

and

$$Q_{\lambda-1/2}^{(1,2)}(\cos\theta) = \frac{1}{2}\left[P_{\lambda-1/2}(\cos\theta) \pm \frac{2i}{\pi} Q_{\lambda-1/2}(\cos\theta)\right] \tag{A-10}$$

where $Q_{\lambda-1/2}(\cos\theta)$ is the Legendre function of the second kind. The uniform asymptotic expansions for $Q_{\lambda-1/2}^{(1,2)}(\cos\theta)$ are

$$Q_{\lambda-1/2}^{(1,2)}(\cos\theta) \sim \left(\frac{\theta}{\sin\theta}\right)^{1/2} \left\{\frac{1}{2}\left[1 + \frac{1}{128\lambda^2}\left(1 - \frac{9}{\sin^2\theta} - 6\frac{\cot\theta}{\theta} + \frac{15}{\theta^2}\right)\right] H_0^{(2,1)}(\lambda\theta) - \frac{1}{16\lambda}\left(\frac{1}{\theta} - \cot\theta\right) H_1^{(2,1)}(\lambda\theta)\right\} \tag{A-11}$$

For $|\lambda|\theta \gg 1$, (A-11) becomes

$$Q_{\lambda-1/2}^{(1,2)}(\cos\theta) \sim \frac{\exp\left[\mp i\left(\lambda\theta - \pi/4\right)\right]}{(2\pi\lambda\sin\theta)^{1/2}},\ |\lambda|\theta \gg 1 \tag{A-12}$$

We employ the uniform asymptotic expansions (A-2), (A-7), and (A-11) to evaluate the values of the special functions at the integration and difference nodes. The non-uniform asymptotic expansions (A-4), (A-5), (A-6), (A-8), and (A-12) are used to derive the expressions with the significant physical meanings, locate the saddle points, and find the proper integration paths.

## REFERENCES


1. Mie, G., "Beiträge zur optik trüber medien, speziell kolloidaler metallösungen," *Annalen der Physik*, Vol. 25, 377–445, 1908.
2. Kong, J. A., *Electromagnetic Wave Theory*, Wiley-Interscience, New York, 1990.
3. Watson, G. N., "The diffraction of electric waves by the earth," *Proceedings of the Royal Society of London. Series A, Containing Papers of a Mathematical and Physical Character*, Vol. 95, 83–99, Oct. 1918.
4. Sommerfeld, A., *Partial Differential Equations in Physics*, Academic Press, New York, 1964.
5. Nussenzveig, H. M., "High-frequency scattering by an impenetrable sphere," *Annals of Physics*, Vol. 34, 23–95, 1965.
6. Rumerman, M. L., "Application of the Sommerfeld-Watson transformation to scattering of acoustic-waves obliquely incident upon cylindrical-shells," *Journal of the Acoustical Society of America*, Vol. 91, 2502–2509, May 1992.
7. Kim, H. T., "High-frequency analysis of EM scattering from a conducting sphere coated with a composite-material," *IEEE Transactions on Antennas and Propagation*, Vol. 41, 1665–1674, Dec. 1993.
8. Shim, J. and H. T. Kim, "An asymptotic solution of EM backscattering from a conducting sphere coated with a composite material," *IEEE Transactions on Antennas and Propagation*, Vol. 52, 1465–1472, Jun. 2004.
9. Paknys, R., "Evaluation of Hankel functions with complex argument and complex order," *IEEE Transactions on Antennas and Propagation*, Vol. 40, 569–578, May 1992.
10. Paknys, R. and D. R. Jackson, "The relation between creeping waves, leaky waves, and surface waves," *IEEE Transactions on Antennas and Propagation*, Vol. 53, 898–907, Mar. 2005.
11. Li, M. K. and W. C. Chew, "A new Sommerfeld-Watson transformation in 3-D," *IEEE Antennas and Wireless Propagation Letters*, Vol. 3, 75–78, Dec. 2004.
12. Valagiannopoulos, C. A., "An overview of the Watson transformation presented through a simple example," *Progress In Electromagnetics Research*, PIER 75, 137–152, 2007.
13. Sen, S. G. and M. Kuzuoglu, "Analysis of high frequency plane wave scattering from a double negative cylinder via the modified Watson transformation and Debye expansion," *Progress*

*In Electromagnetics Research*, PIER 84, 55–92, 2008.

14. Langdon, S. and S. N. Chandler-Wilde, "A wavenumber independent boundary element method for an acoustic scattering problem," *SIAM Journal on Numerical Analysis*, Vol. 43, 2450–2477, 2006.
15. Bruno, O. P. and C. A. Geuzaine, "An O(1) integration scheme for three-dimensional surface scattering problems," *Journal of Computational and Applied Mathematics*, Vol. 204, No. 2, 463–476, Jul. 2007.
16. Davis, C. P. and W. C. Chew, "Frequency-independent scattering from a flat strip with $TE_z$-polarized fields," *IEEE Transactions on Antennas and Propagation*, Vol. 56, 1008–1016, Apr. 2008.
17. Delves, L. M. and J. N. Lyness, "A numerical method for locating the zeros of an analytic function," *Mathematics of Computation*, Vol. 21, 543–560, Oct. 1967.
18. Kravanja, P., T. Sakurai, and M. van Barel, "On locating clusters of zeros of analytic functions," *Bit Numerical Mathematics*, Vol. 39, 646–682, Dec. 1999.
19. Kravanja, P. and M. van Barel, "A derivative-free algorithm for computing zeros of analytic functions," *Computing*, Vol. 63, 69–91, 1999.
20. Kravanja, P., M. Van Barel, O. Ragos, M. N. Vrahatis, and F. A. Zafiropoulos, "ZEAL: A mathematical software package for computing zeros of analytic functions," *Computer Physics Communications*, Vol. 124, 212–232, Feb. 2000.
21. Protopopov, V. V., "Computing first order zeros of analytic functions with large values of derivatives," *Numerical Methods and Programming*, Vol. 8, 311–316, 2007.
22. Press, W. H., S. A. Teukolsky, W. T. Vetterling, and B. P. Flannery, *Numerical Recipes: The Art of Scientific Computing*, Cambridge University Press, 2007.
23. Huybrechs, D., "Multiscale and hybrid methods for the solution of oscillatory integral equations," PhD Dissertation, Department of Computer Science, Katholieke Universiteit Leuven, 2006.
24. Chew, W. C., *Waves and Fields in Inhomogenous Media*, Van Nostrand Reinhold, New York, 1990.
25. Fock, V. A., "Diffraction of radio waves around the earth's surface," *Journal of Physics-USSR*, Vol. 9, 255–266, 1945.
26. Nussenzveig, H. M., "Uniform approximation in scattering by spheres," *Journal of Physics A: Mathematical and General*, Vol. 21, 81–109, Jan. 1988.

27. Abramowitz, M. and I. A. Stegun, *Handbook of Mathematical Functions with Formulas, Graphs, and Mathematical Tables*, Dover Publications, Inc., New York, 1970.
28. Wiscombe, W. J., "Improved Mie scattering algorithms," *Applied Optics*, Vol. 19, 1505–1509, 1980.
29. Olver, F. W. J., "The asymptotic expansion of Bessel functions of large order," *Philosophical Transactions of the Royal Society of London. Series A, Mathematical and Physical Sciences*, Vol. 247, 328–368, Dec. 1954.